J. Fluid Mech. (2014), *vol.* 757, *pp.* 649–664.
doi:10.1017/jfm.2014.491

Expansion wave diffraction over a 90 degree corner

Irshaad Mahomed[1] **and Beric W. Skews**[1,†]

[1]Flow Research Unit, School of Mechanical, Industrial and Aeronautical Engineering, University of the Witwatersrand, Johannesburg, 2050, South Africa

(Received 14 April 2014; revised 18 August 2014; accepted 20 August 2014; first published online 25 September 2014)

The diffraction of an initially one-dimensional plane expansion wave over a 90° corner was explored using experiment and numerical simulation. Unlike studies of shock diffraction, expansion wave diffraction has hardly been documented previously. The planar expansion wave was produced in a shock tube by bursting a diaphragm. Two independent parameters were identified for study: (i) the initial diaphragm shock tube pressure ratio, which determines the strength (pressure ratio) of the expansion, and (ii) the position of the diaphragm from the apex of the 90° corner, which determines the width of the wave. The experimentation only considered variation in the shock tube pressure ratio whereas the simulation varied both parameters. A Navier–Stokes solver with Menter's shear stress transport k–ω turbulence model was found to adequately model the overall flow field. A number of major flow features were identified occurring in the vicinity of the corner. These were: a shear layer that originated by flow separation at the apex of the corner; a vortex within a separation bubble that remained attached to the wall, in sharp contrast to what happens in the shock wave diffraction case, where the vortex convects downstream; and a reflected compression wave arising from perturbation signals generated by the diffraction. For a narrow-width expansion wave existing prior to diffraction, the reflected compression wave steepens into an outwardly propagating, weak cylindrical shock wave. Regions of supersonic flow are identified surrounding the bubble and can extend downstream depending on the pressure ratio. Another major flow feature identified in some cases was an oblique shock located near the separation bubble. A large wake region is evident immediately downstream of the bubble and appears to consist of two distinct layers. The experimental results showed large-scale turbulent structures within the separation bubble, and shear layer instability and vortex shedding from the separation bubble were also evident.

Key words: compressible flows, gas dynamics, shock waves

1. Introduction

Whilst there have been many studies of unsteady two-dimensional shock wave diffraction around sharp corners over the past forty years, since the early work of Skews (1967), there have not been any equivalent and comparative studies for

† Email address for correspondence: beric.skews@wits.ac.za

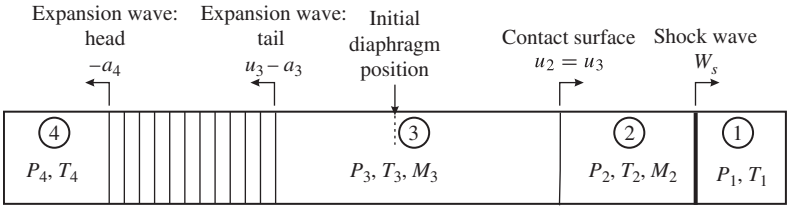

FIGURE 1. Flow features and regions in a simple shock tube after diaphragm burst.

expansion waves. The earliest reference to expansion wave diffraction found is that of Powell (1957), for a complete wave, i.e. into vacuum, which was extended by Anderson (1967) for an incomplete wave such as occurs in a shock tube. These, however, deal with a small change in the direction of the wall, thus for very small corner turning angles. Most textbooks on compressible flow, such as Anderson (2003), treat the one-dimensional unsteady propagation of expansion waves in some detail. This is normally in the context of a piston accelerating down a tube, and includes the special case of a centred wave for initial infinite acceleration followed by constant velocity, which is the case conventionally assumed for the shock tube case resulting from a bursting diaphragm. Some analysis and experiments of the one-dimensional expansion wave behaviour in terms of the initial conditions in a shock tube are given in Billington (1956) and Glass & Sislean (1994), and in more detail below.

1.1. *One-dimensional expansion waves in a shock tube*

A schematic of the flow features in a simple shock tube following diaphragm burst is shown in figure 1. Initially the diaphragm separates regions 1 and 4, with high pressure P_4 on the left, in the driver section, and low pressure, P_1, in the driven section, with the diaphragm pressure ratio written as $P_{41} = P_4/P_1$. After diaphragm burst, a shock wave propagates into region 1, raising the pressure and temperature to a shock strength of P_{21} and Mach number M_2. An expansion wave propagates into the driver section, expanding the gas into region 3. Regions 2 and 3 are separated by a contact surface across which the pressures and velocities are the same, $P_3 = P_2$ and $u_3 = u_2$, but the Mach numbers are different, $M_3 \neq M_2$. The expansion wave spreads out in time, with the head propagating at the speed of sound in region 4, a_4, and the tail at the speed of sound in region 3, a_3, relative to the gas, which is moving at velocity u_3 to the right. As shown in the figure, the tail is moving to the left when $a_3 > u_3$; but if the reverse is true, then it will move to the right from the diaphragm position, which occurs for sufficiently large diaphragm pressure ratios. This will be treated in more detail subsequently.

By taking the unsteady equations for a one-dimensional expansion wave with those for a moving shock and applying the matching conditions that $P_3 = P_2$ and $u_3 = u_2$, the basic shock tube equation is derived (Anderson 2003), with γ being the ratio of specific heats:

$$\frac{P_4}{P_1} = \frac{P_2}{P_1}\left[1 - \frac{(\gamma_4 - 1)\left(\dfrac{a_1}{a_4}\right)\left(\dfrac{P_2}{P_1} - 1\right)}{\sqrt{2\gamma_1\left[2\gamma_1 + (\gamma_1 + 1)\left(\dfrac{P_2}{P_1} - 1\right)\right]}}\right]^{-2\gamma_4/(\gamma_4 - 1)}. \tag{1.1}$$

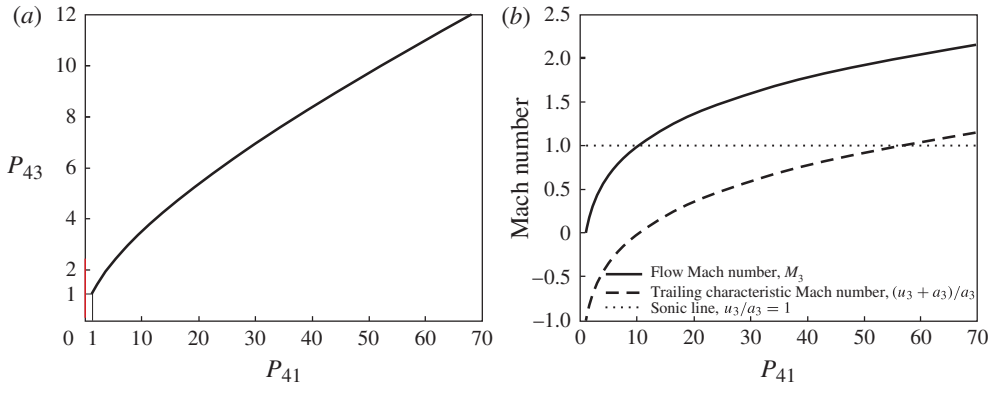

FIGURE 2. Variation of expansion wave pressure ratio, P_{43}, and Mach numbers with diaphragm pressure ratio, P_{41}.

Thus, since $P_3 = P_2$, the pressure ratio for the expansion wave, $P_{43} = P_4/P_3$, is

$$\frac{P_4}{P_3} = \frac{P_4/P_1}{P_2/P_1}. \tag{1.2}$$

By applying isentropic relations, other ratios, such as for temperature and density, may be obtained. For the case under consideration in this paper, it will be taken that the same gas (air with $\gamma = 1.4$) and at the same initial temperature, $a_1 = a_4$, will be used on either side of the diaphragm, as in the experiments.

The variation of the expansion wave pressure ratio with the diaphragm pressure ratio is given in figure 2. For a fixed driven section pressure and increasing driver pressure, i.e. increased P_{41}, which is common in shock tube operation, the expansion pressure ratio, P_{43}, increases but at a slower rate. Consider a left-running expansion wave propagating into a quiescent stagnant gas, as shown in figure 1. A particle traversed by the leading characteristic will experience acceleration until the particle has reached the trailing characteristic and a velocity u_3. Also, there occurs a reduction in temperature within the expansion wave; therefore the flow Mach number would continually increase between the leading and trailing characteristics. Sonic and supersonic flow is possible at some location within the expansion waves. If the expansion wave occurs in a shock tube of constant cross-sectional area, then the flow between the trailing characteristic and the contact surface will be uniform. It is pertinent to establish the diaphragm pressure ratio that would establish sonic flow at the trailing characteristic.

Interesting conditions emerge from these figures. Very high diaphragm pressure ratios are needed for the trailing characteristic to go supersonic, where it is moving at local sonic velocity in a gas that itself is moving supersonically. A diaphragm pressure ratio of 56 is predicted for the trailing wave to go sonic relative to ground, the flow Mach number then being $M_3 = 2$. A more interesting and practically achievable case is where the gas in region 3, M_3, goes sonic. The trailing characteristic will then remain stationary at the position of the diaphragm, since its velocity is $u_3 - a_3$ and $u_3 = a_3$. For this to occur, a diaphragm pressure ratio of $P_{41} = 10.4$ is required.

In performing experiments on expansion waves, one of the issues, which make it even more demanding experimentally than the study of shock waves, is that the

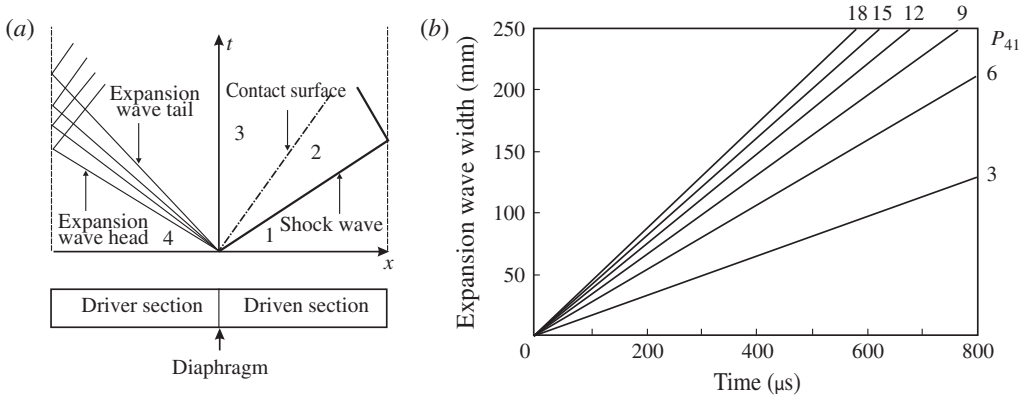

FIGURE 3. Shock tube distance–time (x, t) wave diagram, and effect of diaphragm pressure ratio on expansion wave width for initial gas temperatures $(T_1 = T_4)$ of 300 K.

Diaphragm pressure ratio	Unit Reynolds number
3	1.94×10^7
6	5.26×10^7
9	8.65×10^7
12	1.20×10^8
15	1.54×10^8

TABLE 1. Reynolds number per unit length behind the expansion wave.

width of the wave and thus the changes of variables within it vary in both space and time. In addition, the test section would need to be positioned in the high-pressure driver section rather than the low-pressure driven section. Consider the standard shock tube x–t wave diagram in figure 3. For a given distance of the test section from the diaphragm position, both the width and duration of the passage of the expansion wave will depend on the initial diaphragm pressure ratio. Assuming that the initial temperature in the driver and driven sections is 300 K, the arrival of the expansion wave head may easily be determined, and then the width of the expansion wave, as illustrated in the figure.

It is not uncommon for test pieces to be placed in the driven section of shock tubes, not only to examine shock wave interactions, but also to use the flow in region 2 as a short-duration wind tunnel. For such a test position, region 3 is less useful owing to passage over the remnants at the diaphragm station. However, for the current arrangement with the test section in the driver, it is of interest to determine the associated flow Reynolds number in region 3 if it were to be used in a similar fashion. The Reynolds numbers are given on a unit length basis in table 1 and are computed for a range of diaphragm pressure ratios using viscosity from the Sutherland law.

2. Method

The basic geometry decided on for both experiment and numerical simulation was to have a test section in the driver section fitted with a 90° diffraction corner.

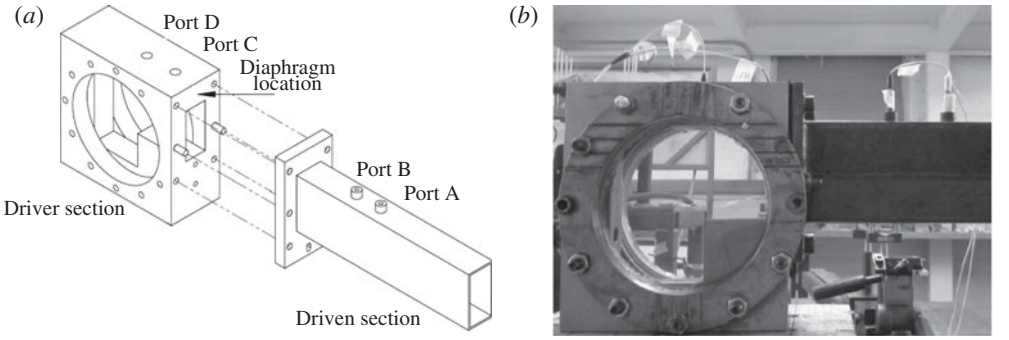

FIGURE 4. Details of experimental rig.

Sufficient volume had to be allowed below the corner since the flow induced by the expansion wave would be up towards the corner, around it and then along the main shock tube towards the driven section.

2.1. *Experimental rig*

As indicated above, in order to keep the width of the expansion wave within reasonable limits, considering visualisation constraints, the diffraction corner needs to be close to the diaphragm position. This placed severe limits on the rig design, resulting in only one diaphragm position being used, with the testing confined to only varying the diaphragm pressure ratio. For experimentation, the driven section was exposed to ambient conditions of 83.4 kPa and a temperature of 288 K. Gauge pressures used in the driver section were 1.8, 3.6, 4.6 and 5.6 bar, giving diaphragm pressure ratios of 3.2, 5.6, 6.5 and 7.7, respectively. The shock tube was 90 mm high and 40 mm wide and the distance of the corner from the diaphragm position was 83 mm. The rig arrangement is given in figure 4 (note that the photograph is a flipped image to satisfy the convention that flow in shock tubes is from left to right). Two transducers were positioned in the driven section for determination of shock speed, and two in the driver section, one immediately above the diffraction corner. Two cameras were used for shadowgraph imaging: a Nikon D40 DSLR 10 MP digital still camera, and a Photron SA5 high-speed camera operated at 0.125 Mpx and 60 000 frames per second.

2.2. *Numerical simulation*

Considerable reliance had to be placed on simulation results because of the experimental limitations of the rig in terms of diaphragm positioning and pressure ratio, and since schlieren and shadow photography did not clearly resolve the expansion wave, so its position could not be determined. The simulations were thus done to vary P_{41} beyond that achieved by experimentation. The range was chosen as: 3, 6, 9, 12, 15 and 18. (The maximum for the experiment was 8.4.) For each value of diaphragm pressure ratio, the distance of the diaphragm from the corner, D, was set to 0, 10, 40 and 70 mm. (The value of D for the experiment was constant at 83 mm.)

Two computational flow domains were generated. The first, or experimental, domain was to validate the user set-up of the simulation code using experimental data. This

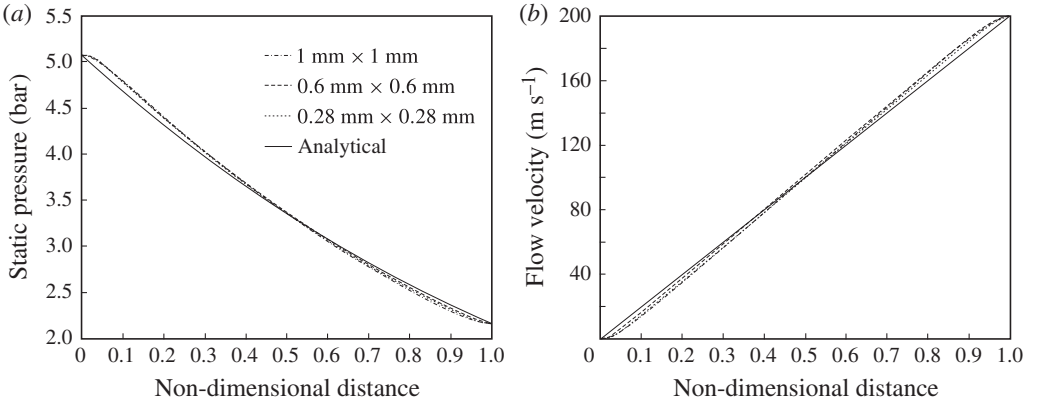

FIGURE 5. Theoretical and numerical flow properties through a one-dimensional centred expansion wave.

domain was based on the physical dimensions of the rig and subsequently was constrained to a short simulation time. This constraint was a consequence of the reflection of the diffracted expansion waves from the shock tube walls and their arrival into the region of study, thus leading to rig-dependent effects. To generate longer test times, a larger domain was employed. The simulation code employed was ANSYS FLUENT V.13 using both Euler and the Reynolds-averaged Navier–Stokes (RANS) equations, for two-dimensional flow with air as an ideal gas.

Since theoretical solutions of flow properties through a one-dimensional isentropic centred expansion exist, such as in a shock tube, this was an obvious initial test case for checking grid independence using an Euler simulation. Rather interesting results are shown in figure 5. The calculated curves show curvature at the head and tail of the wave in order to meet smoothly with the uniform states on either side, i.e. for the derivatives to be continuous. The theory, however, has these derivatives as discontinuous across these characteristic lines and gives an infinite acceleration across the head of the wave and similarly an infinite deceleration across the tail. This would not be the case in real flows, as also indicated in the simulations. Changing cell size as shown in the figure gives minor differences, with the 0.6 mm $\times$ 0.6 mm cell size giving the closest agreement away from the end points. A similar study of the diffracted wave on the vertical wall indicated that an original mesh of 0.6 mm $\times$ 0.6 mm with two levels of refinement is sufficiently resolved.

In order to account for boundary layer effects, Menter's shear stress transport (SST) k–ω turbulence model was implemented. This model was selected for its versatility and potential to model turbulent boundary layer flow and free stream turbulence. This necessitated special requirements for the mesh topology at locations where boundary layers would develop. The mesh was refined near the wall as shown in figure 6 for 20 mm closest to the corner, sufficient to satisfy the $y+$ condition that $5 \leqslant y+ \leqslant 30$.

3. Results

The majority of this section deals with results where the flow Mach number behind the trailing characteristic was subsonic ($M_3 < 1$). This occurs for $P_{41} < 10.4$ in air. These results were obtained through a combination of experiment and simulation, from which the primary (major) flow features are identified. This is followed by a

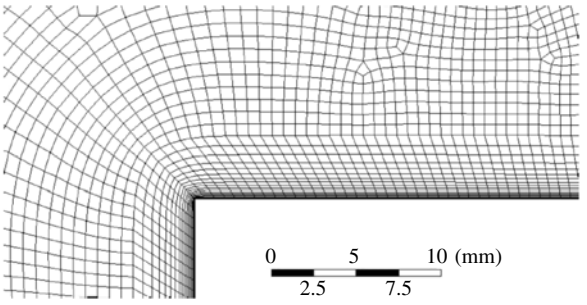

FIGURE 6. Grid topology for the Navier–Stokes solver for 20 mm from the corner.

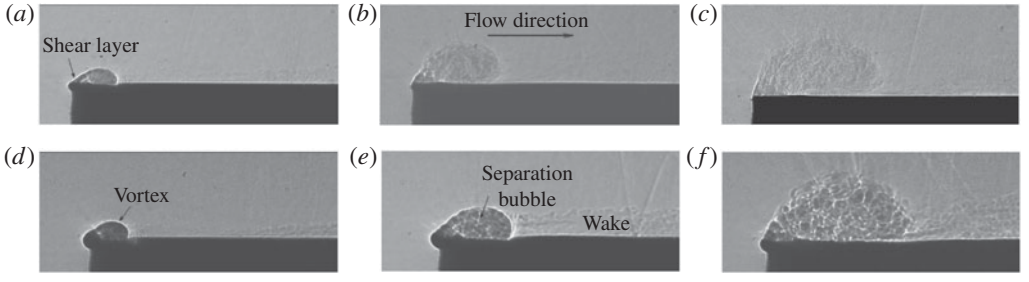

FIGURE 7. Typical shadowgraph images: (*a–c*) $P_{41} = 3.2$; (*d–f*) $P_{41} = 7.7$. Time delays: (*a*,*d*) $t_f = 200$, (*b*,*e*) 400 and (*c*,*f*) 600 μs.

detailed discussion for each primary flow feature with variation in the two independent parameters, D and P_{41}. Lastly, simulation results for $M_3 \geqslant 1$ are discussed. The zero reference position in time, t_f, was taken at the instant when the leading characteristic of the incident expansion wave arrived at the 90° corner, i.e. from the time that the diffraction around the corner starts.

3.1. *Major flow features*

Selected shadowgraph images from tests using the high-speed camera are given in figure 7 for two diaphragm pressure ratios. Major flow features are labelled on the images. The arrow indicates the direction of flow back up the shock tube towards the diaphragm station, taken as positive to the right. Simulation results are given in figure 8 for the same pressure ratios. For stronger waves and later times, shock waves appear in the flow and will be treated in § 3.4. From the above experiment and simulation results, the following major flow features are identified: a shear layer originating at the diffraction corner; a separation bubble attached to the horizontal wall and enclosing circulatory fluid (vortex), which is markedly different from what happens in shock wave diffraction; turbulent structures within the separation bubble; and a region of flow immediately downstream of the separation bubble of unclear internal structure, termed the wake region. In figure 7, for $P_{41} = 7.7$ and at 200 and 400 μs time delay, a distinct bulge appeared at the diffraction corner and is significantly less pronounced for $P_{41} = 3.2$. This effect is probably due to the deflection angle of incident light rays, where the deflection angle exceeded the measuring range of the visualisation system owing to the very high density gradients.

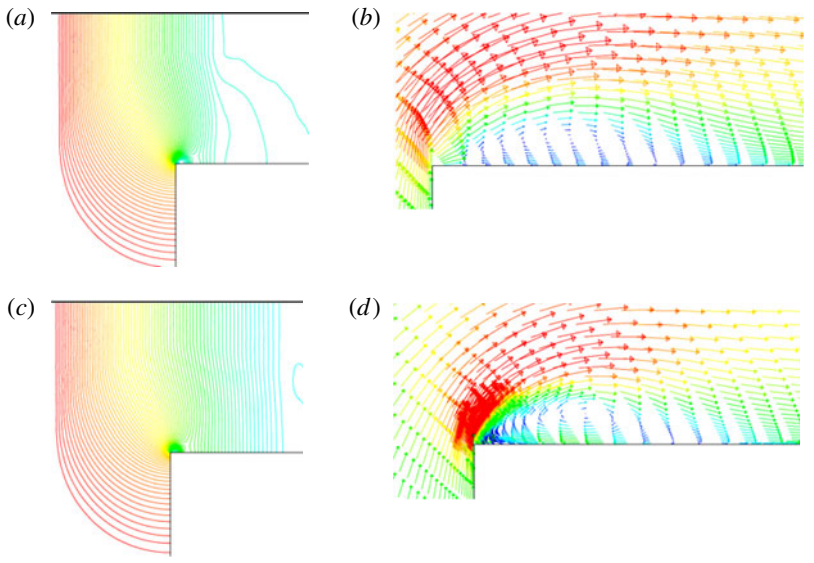

FIGURE 8. Pressure contours and velocity vector plots for (*a*,*b*) $P_{41} = 3.2$ and (*c*,*d*) $P_{41} = 7.7$, at $t_f = 150$ μs.

A reflected wave arising from the corner and propagating back up into the advancing expansion wave and induced flow is evident in the simulations shown in figure 8. In the lower image, for $P_{41} = 7.7$, this reflected wave is fully contained within the expansion wave. The reflected wave is not resolved in the experiment owing to the low density gradients and insufficient sensitivity of the visualisation set-up. On the other hand, turbulent flow features identified in the experiment were not evident in the simulation, where strong circulatory vortex patterns are evident, details of which will be dealt with later.

3.2. *The diffracted and reflected waves*

The diffraction of a single element of the expansion wave at the 90° corner generates a reflected perturbation signal that propagates radially outwards as a reflected compression wave. In comparison, for shock wave diffraction with a subsonic post-shock condition, a reflected expansion wave propagates radially outwards into a region of uniform flow (Skews 1967) and is circular in profile. However, in the current expansion wave case, the reflected compression wave propagates into regions of uniform flow beyond the trailing characteristic and a region of non-uniform flow within the expansion wave itself, depending on the width of the incident one-dimensional expansion wave prior to diffraction, as is evident in figure 8. It is shown above that the diaphragm pressure ratio (P_{41}) and the propagation time of the incident expansion wave prior to diffraction influence the wave's width, and thus the distance between the diaphragm location and the diffraction corner (D) has an influence on the diffraction process.

The influence of the diaphragm position is given in figure 9 for $t_f = 350$ μs, showing that the compression wave can steepen up to become a shock wave. The reason the one-dimensional part of the wave gets wider as D increases is that the reference time, t_f, is for the leading characteristic to move from the corner, and not

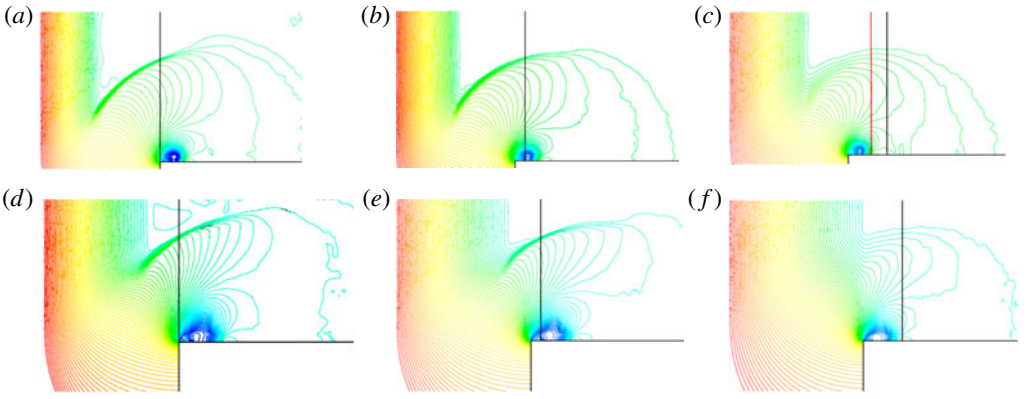

FIGURE 9. Pressure contours for (*a–c*) $P_{41} = 3$ and (*d–f*) $P_{41} = 6$, with $D = 0$, 10 and 40 mm, at $t_f = 350$ μs. The vertical black line is the initial diaphragm position.

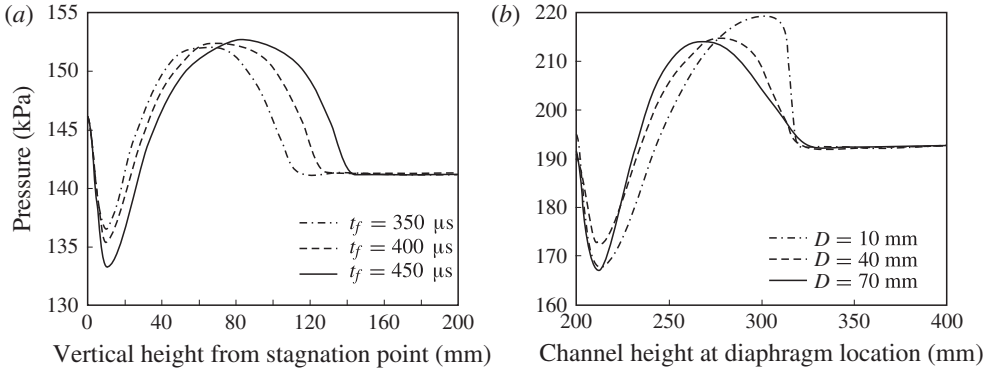

FIGURE 10. Vertical pressure distribution. (*a*) Growth of the reflected pressure with time for $P_{41} = 3$, $D = 40$ mm. Data are along a vertical line starting at the stagnation point on the horizontal wall. (*b*) Pressure distribution on a vertical line at the diaphragm station for $P_{41} = 6$ and different diaphragm positions.

from the diaphragm position. The case for $D = 0$ mm is particularly interesting since the incident expansion wave does not propagate over the diffraction corner at all, having been generated at the corner. This is true as long as the gas velocity at the trailing edge is subsonic. As shown above, if the flow is supersonic, $P_{41} \geqslant 10.4$, the trailing characteristic will move to the right, and is discussed in § 3.5. It is evident that, the further the diaphragm is from the corner, the longer it will take for the reflected compression waves to consolidate into a shock wave.

The pressure variation along a vertical line starting at the stagnation point behind the separation bubble on the horizontal wall (refer to the red line in the top-right image of figure 9) is given in figure 10(*a*). The pressure first drops rapidly as a result of the influence of the adjacent vortex, then increases to a maximum two-thirds up the line, before dropping to the pressure in the uniform region behind the expansion tail. Steepening into a shock depends on the diaphragm distance, as illustrated in figure 10(*b*). A combination of large values of P_{41} (6 and 9) and D (40 and 70 mm) generates a broad expansion wave prior to diffraction and this would delay the

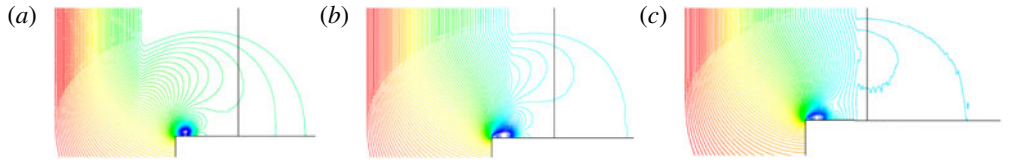

FIGURE 11. Pressure contours for (*a*) $P_{41} = 3$, (*b*) $P_{41} = 6$ and (*c*) $P_{41} = 9$, with $D = 70$ mm and $t_f = 400$ μs.

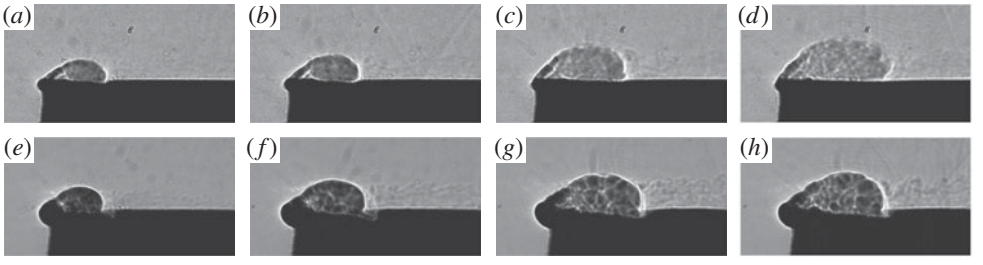

FIGURE 12. Shadowgraph images for (*a–d*) $P_{41} = 3.2$ and (*e–h*) $P_{41} = 7.7$ at times of (*a*,*e*) 200, (*b*,*f*) 250, (*c*,*g*) 300 and (*d*,*h*) 350 μs, respectively.

formation of a cylindrical shock wave. On the other hand, variation of pressure ratio has a minimal effect on the steepening of the compression wave as shown in figure 11.

3.3. *The separation bubble*

The formation of the separation bubble is illustrated through shadowgraph images in figure 12 for $P_{41} = 3.2$ and 7.7. The flow separates at the corner, followed by a clearly developed vortex structure, with a shear layer extending into the flow. This layer appears to reattach at some finite distance downstream from the diffraction corner, and forms the outer periphery of the separation bubble. This is in marked contrast to the case of shock diffraction (Skews 1967), where the vortex propagates away from the wall. As expected, the bubble grows over time and the growth is significantly larger for $P_{41} = 7.7$ than for 3.2. Also, at $P_{41} = 7.7$ a faint transonic shock is indicated just above the shear layer for time delay values at 300 and 350 μs, and will be discussed later. At early time there appears a clearer area between the shear layer and the rotating vortex, examined in more detail below. Flow separation was not as easily identified at higher values of P_{41} owing to relatively steep density gradients. Information at the corner itself is obscured because the limits of the optical system were exceeded, resulting in a dark area due to these very high density gradients, which masks the details at the corner. This also gives the impression of the flow overlapping the horizontal wall.

Small shocklets, identified as short white lines emanating a finite distance into the flow field from ridges in the shear layer, are evident for case of the higher pressure ratio. These ridges are an indication of shear layer instability. Shocklets were not observed in the simulation data, since the shear layer profile was resolved as a smoothly contoured surface with no ridges. It could not be ascertained if the shocklets are a localised effect on the shear layer or spanned the width of the test section. The lack of clarity may be due to some transverse flow variability.

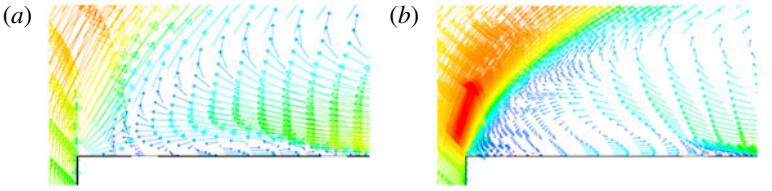

FIGURE 13. Flow at the corner for (*a*) $P_{41} = 3.2$ and (*b*) $P_{41} = 7.7$ at time of 320 μs, $D = 83$ mm.

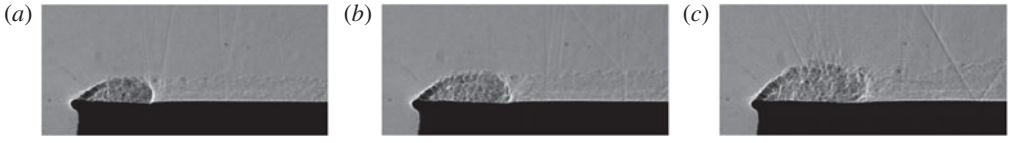

FIGURE 14. Shadowgraphs for $P_{41} = 6.5$, with (*a*) $t_f = 300$, (*b*) 350 and (*c*) 400 μs, $D =$ 83 mm.

Further clarity of the flow in the vicinity of the corner is examined through simulation. It is well known that in the shock wave diffraction case a small vortex, known as a viscous vortex (since it does not appear in Euler simulations), occurs at the corner due to the upstream boundary layer flow around the corner. A similar effect is expected to occur in the expansion wave case. Simulations corresponding to the experimental boundary conditions are shown in figure 13 in the vicinity of the corner. A small counter-rotating vortex is evident, corresponding to the indications in the experiment. The primary vortex does appear in Euler simulations, as it does in shock wave diffraction, due to the baroclinic effect.

The shear layer and 'wake' region were identified in § 3.1 using shadowgraph images for $P_{41} = 3.2$ and 7.7. Figure 12 illustrated the flow field near the diffraction corner. At early times the shear layer maintained a smoothly curved profile over the upper periphery of the separation bubble. This smooth profile was present up to a certain time, after which the shear layer developed an instability similar to that experimentally observed in shock diffraction at late times (Skews *et al.* 2012). Vortex shedding also becomes evident at later times. Figure 14 shows a distinct pattern of vortices convecting downstream. At later times, these shed vortices dissipate in the turbulent downstream wake. The third image from this test also has indications of shocklets on the upper surface of the bubble.

In all the shadowgraph images presented thus far, a wake region is evident immediately downstream of the separation bubble. It was found, through schlieren imaging with a horizontal knife edge, that certain flow structures were better resolved than for the shadowgraph results. These results are shown in figure 15. The wake region appears to comprise two distinct layers. The lower layer was observed to develop linearly on the horizontal wall at a finite distance downstream of the separation bubble and appeared embedded within the second layer. The exact nature of this wake flow is not known and is not indicated in the simulation. Further work both in experimentation and in simulation, using large eddy simulation (LES), for example, will be required. It should be noted that the experiment is in a test section of finite width, that both transverse effects and the influence of the window surfaces need to be considered, and that the diaphragm is initially slightly curved.

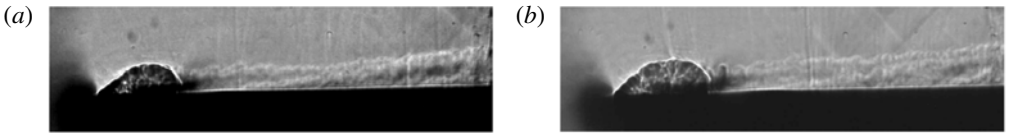

FIGURE 15. Schlieren imaging with a horizontal knife edge highlighting the structure in the wake region for $P_{41} = 6.5$ and (*a*) $t_f = 300$ and (*b*) 350 μs, $D = 83$ mm.

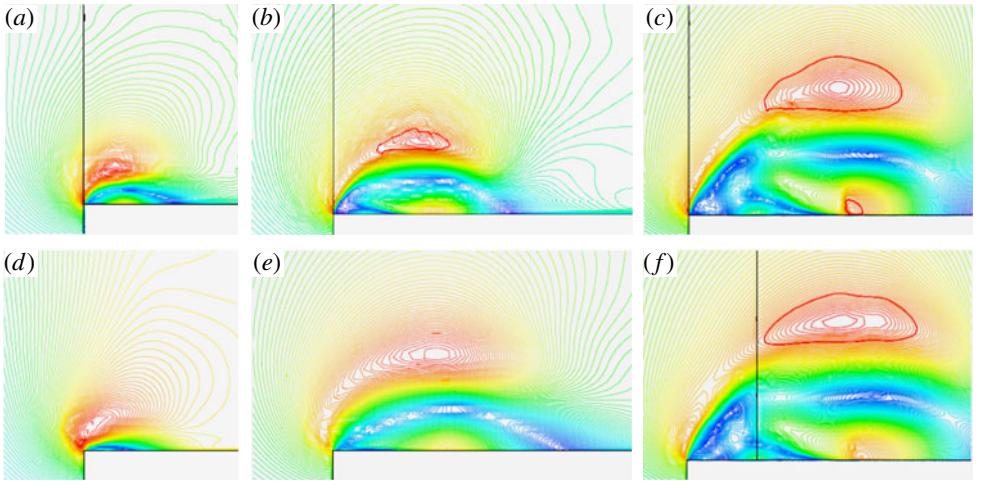

FIGURE 16. Mach number contours for $P_{41} = 3$ and (*a–c*) $D = 0$ and (*d–f*) 40 mm. Simulation times t_f: (*a*,*d*) 100, (*b*,*e*) 300 and (*c*,*f*) 600 μs. Sonic line highlighted.

3.4. *Local supersonic regions and associated shock waves,* $P_{41} \leqslant 10.4$

The high-resolution shadowgraph images obtained experimentally for $P_{41} = 7.7$ gave a strong indication of the existence of supersonic flow and shocks above the separation bubble. Limitations in the experiment, in terms of both test section size (owing to waves reflected off the test section surfaces limiting test time) and the magnitude of achievable diaphragm pressure ratio, meant that the above indications could only be explored through simulation at this stage. The main parameters are the pressure ratio, P_{41}, the diaphragm distance, D, and the time, t_f.

The development and evolution of a supersonic patch above the separation bubble, due to flow acceleration over the curved surface, is shown in figure 16, for a low pressure ratio of 3. The outline of the patch is highlighted with a sonic line. For $D = 0$ there is no patch at $t_f = 100$ μs but it develops at later times, such as at $t_f = 300$ μs, and continues to grow thereafter. For larger values of D it develops later on, between times of 300 and 600 μs. For larger values of D and the same pressure ratio and time, the expansion wave is wider and the gradients less steep. The absolute Mach number for the flow in this region varied from transonic to strong supersonic speeds. The flow near the upper periphery of the separation bubble expanded supersonically and then decelerated back to subsonic speeds in the absence of a shock wave. This phenomenon was also observed for a case of shock diffraction over a 90° corner by Kleine, Ritzerfeld & Grönig (2003). An interesting feature for $D = 0$ and $t_f = 600$ μs, which is discussed below, is the appearance of a small supersonic patch within the separation bubble and close to the wall.

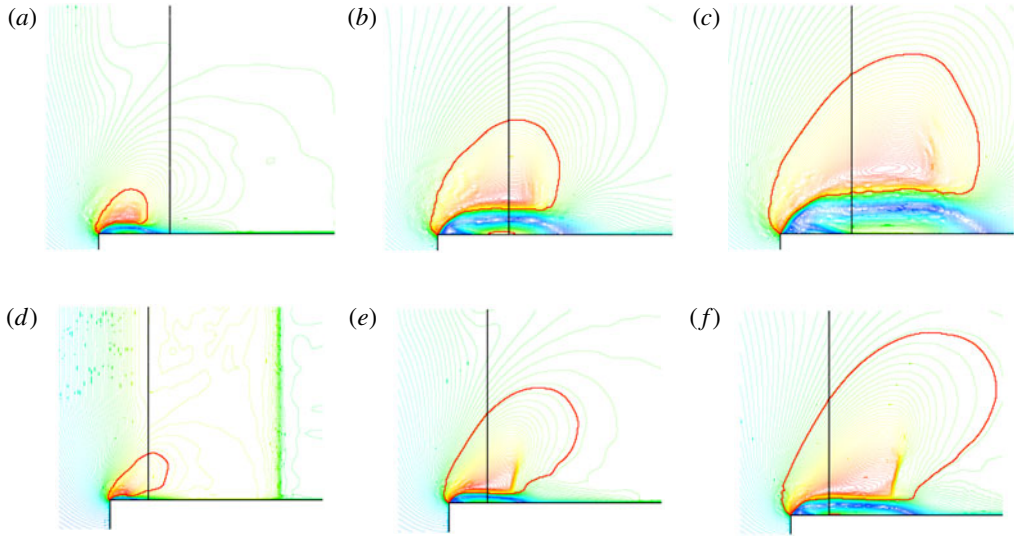

FIGURE 17. Mach number contours for (*a–c*) $P_{41} = 6$ and (*d–f*) $P_{41} = 9$, for $D = 10$ mm. Simulation times t_f: (*a*,*d*) 100, (*b*,*e*) 200 and (*c*,*f*) 300 μs. Sonic line highlighted. Results for $P_{41} = 9$ are zoomed out compared to the $P_{41} = 6$ case.

However, for higher pressure ratios some new features appear. Figure 17 shows results for $P_{41} = 6$ and 9 at early times. The supersonic patch grows and extends all the way to the corner compared to the $P_{41} = 3$ case, and becomes less symmetrical with increasing Mach number to the right. For the $P_{41} = 9$ case at 200 μs, an oblique shock develops towards the rear of the patch and just above the separation bubble. Indications are that at 300 μs this shock develops a lambda configuration. The shocks are not normal to the flow and must be oblique since the flow just downstream remains supersonic.

These new features will develop even further at later times. Figure 18 compares the flows at $t_f = 600$ μs for different diaphragm positions. For $P_{41} = 6$ and $D = 0$ and 40 mm, no oblique shock was present; rather, a compression fan develops towards the rear end of the separation bubble. This compression fan would, at a later stage, coalesce into a shock. At $D = 70$ mm the oblique shock was evident at the base of the separation bubble extending a finite height into the supersonic region and then terminating as a compression fan.

It is again noted that in some cases there is an additional supersonic patch within the separation bubble and adjacent to the wall. Figure 19 presents enlarged views for the following two cases: figure 16(*c*) for $P_{41} = 3$, and figure 18(*c*), both for $t_f = 600$ μs and $D = 40$ mm. In the first case the supersonic region was terminated by a shock, termed a recompression shock. This shock is similar to that observed in a case of shock diffraction over a backward-facing step (Kleine *et al.* 2003). The recompression shock was observed to occur for small D and $P_{41} = 3$ only. For the higher pressure ratio, the patch is elongated, as is the separation bubble. It is also noted that the flow near the corner for these larger diaphragm pressure ratios is somewhat different from that in figure 13. In both cases shown in figure 19 the flow separates just after the supersonic patch and a second small counter-rotating vortex develops next to what was previously referred to as the viscous vortex.

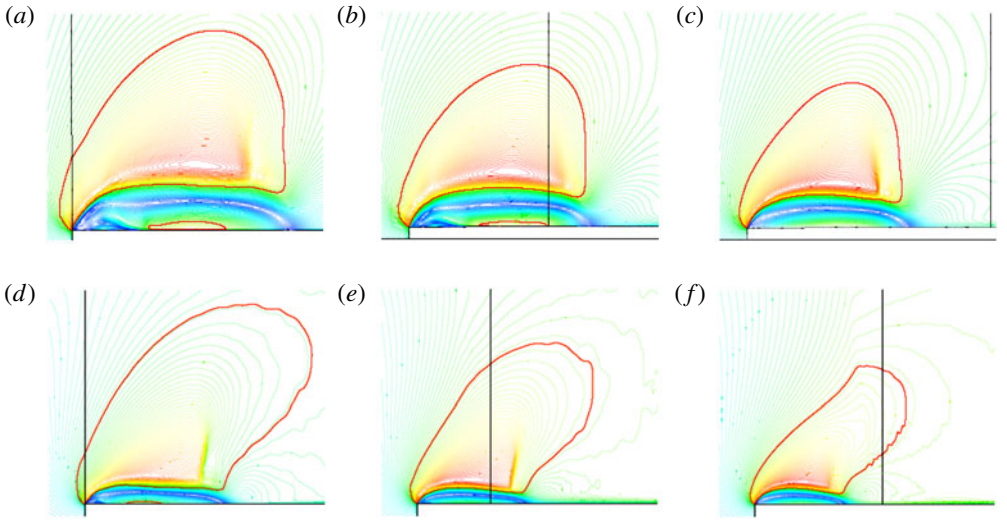

FIGURE 18. Mach number contours for (*a–c*) $P_{41} = 6$ and (*d–f*) $P_{41} = 9$, for (*a*,*d*) $D = 0$, (*b*,*e*) 40 and (*c*,*f*) 70 mm. Simulation time $t_f = 600$ μs. Sonic line highlighted. Results for $P_{41} = 9$ are zoomed out compared to the $P_{41} = 6$ case.

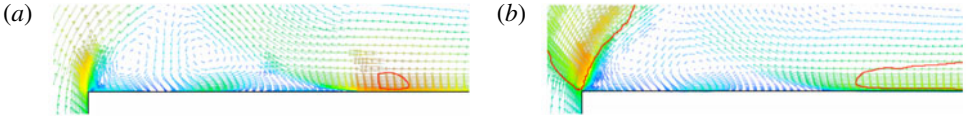

FIGURE 19. Mach number contours for (*a*) $P_{41} = 3$ and (*b*) $P_{41} = 6$, with $t_f = 600$ μs and $D = 40$ mm.

3.5. *Supersonic flow conditions,* $P_{41} \geqslant 10.4$

When the whole of region 3 between the trailing edge of the expansion wave and the contact surface in a shock tube is supersonic, the position and shape of the sonic line will necessarily change and will be positioned in the contact surface on the downstream side of the domain when M_3 is supersonic and M_2 still subsonic. The cases reported on are for $P_{41} = 12$ and 15. Both Euler and Navier–Stokes simulations were run and the flows outside of the bubble and away from the wall were very similar. The gross shape of the separation bubble, for both solvers, was elongated, thin and attached to the horizontal wall. The flow patterns for various diaphragm positions is given in figure 20. The shock structure changes depending on the width of the expansion at a given time and thus on the distance between the diaphragm and the corner. In the one-dimensional portion of the expansion wave, unaffected by the presence of the corner, the sonic line is on the stationary characteristic at the position of the diaphragm. The characteristics to the right are embedded in the supersonic flow and move upstream. The effect of the corner modifies the position of the sonic line by pushing it to the right as the compression wave moves the subsonic portion of the flow forwards, but remains facing into the flow near the corner due to the acceleration around the separation bubble. The sonic line also always lies above the subsonic flow adjacent to the wall. A small subsonic patch is also present just behind

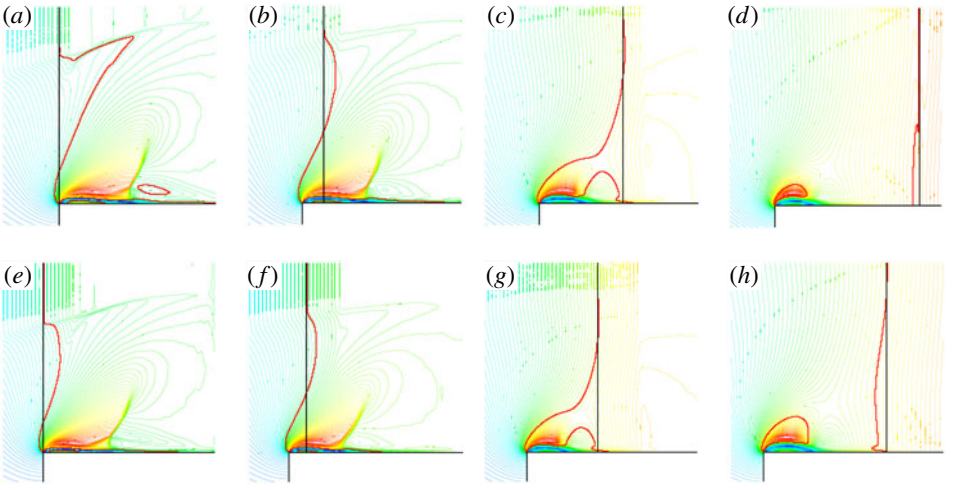

FIGURE 20. Mach number contours for (*a–d*) $P_{41} = 12$ and (*e–h*) $P_{41} = 15$, with $t_f =$ 600 μs and (*a*,*e*) $D = 0$, (*b*,*f*) 10, (*c*,*g*) 40 and (*d*,*h*) 70 mm. Sonic line highlighted.

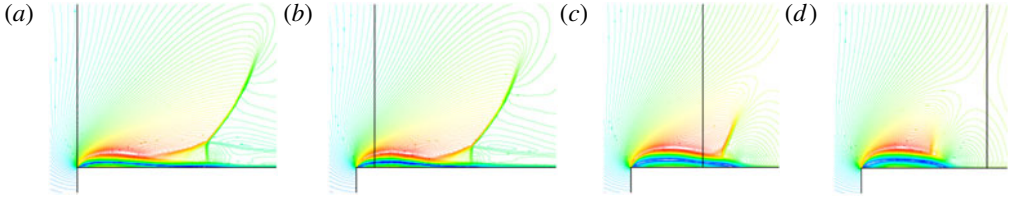

FIGURE 21. Mach number contours for $P_{41} = 15$ with $t_f = 600$ μs and (*a*) $D = 0$, (*b*) 10, (*c*) 40 and (*d*) 70 mm.

the oblique shock for $D = 0$ and $P_{41} = 12$. For large D the supersonic patch around the bubble separates from the main supersonic area within the main expansion wave.

Enlargements to show details of the shock patterns are given in figure 21 for $P_{41} =$ 15 and different diaphragm positions. For small D the lambda geometry is generated with a clearly defined three-shock intersection and a shear layer emanating from the triple point. A normal shock connects the triple point to the wall. The wave system gets weaker and weaker as D increases until it becomes a compression wave at $D =$ 70 mm.

4. Conclusion

The overall behaviour of a one-dimensional expansion wave propagating over a 90° corner has been established. The flow features are dependent on the pressure ratio across the wave, as well as its width as it passes over the corner, which depends on the distance from the corner where it is initiated by a bursting diaphragm.

The major flow features are identified through high-resolution shadowgraph images and numerical simulation. As flow is initiated around the corner, a shear layer develops enclosing a separation bubble with a vortex core. The vortex remains attached to the wall, in contrast to shock diffraction, where the shear layer rolls up into a vortex that propagates away from the wall. The experiment showed complex

turbulent structure within the separation bubble as well as a turbulent wake developing downstream.

As the expansion wave propagates over the corner, a reflected compression wave propagates back into the flow. Under some circumstances this compression wave steepens into a shock wave.

Regions of supersonic flow are generated above the separation bubble, and in some cases an oblique shock wave structure can also be generated towards the rear end of the bubble. In a few instances a small supersonic patch develops very close to the wall within the separation bubble, and a small shock can also develop, similar to the embedded shocks that can occur in the vortex in shock diffraction. The numerical simulation indicated complex flows within the bubble consisting of secondary vortices and local flow separation.

Many of the features found have not been fully investigated, and differences between simulation and experiment clearly require further investigation. These may be related to possible three-dimensional effects in the experiment and different simulation codes, such as LES, to be implemented. Experiments also need to be established for higher diaphragm pressure ratios, particularly for the case where the flow that trails the expansion wave is supersonic.

Acknowledgements

We are grateful for the financial support of the South African National Research Foundation, and that through the Fluxion bursary scheme of Armscor.

REFERENCES

ANDERSON, W. M. 1967 Diffraction of an incomplete expansion wave by a corner. *Proc. Camb. Phil. Soc.* **63**, 909–921.

ANDERSON, J. 2003 *Modern Compressible Flow with Historical Perspective*. McGraw-Hill.

BILLINGTON, I. J. 1956 An experimental study of one-dimensional refraction of a rarefaction wave at a contact surface. *J. Aeronaut. Sci.* **23**, 997–1006.

GLASS, I. I. & SISLEAN, J. P. 1994 *Nonstationary Flows and Shock Waves*. Oxford University Press.

KLEINE, H., RITZERFELD, E. & GRÖNIG, H. 2003 Shock wave diffraction at a ninety degree corner. *Comput. Fluid Dyn. J.* **12**, 142–158.

POWELL, J. B. L. 1957 The diffraction of a rarefaction wave by a corner. *J. Fluid Mech.* **3**, 243–254.

SKEWS, B. W. 1967 The perturbed region behind a diffracting shock wave. *J. Fluid Mech.* **29**, 705–719.

SKEWS, B., LAW, C., MURITALA, A. & BODE, S. 2012 Shear layer behaviour resulting from shock wave diffraction. *Exp. Fluids* **52**, 417–424.